Available online at www.sciencedirect.com

ScienceDirect

Geochimica et Cosmochimica Acta 173 (2016) 181–197

Geochimica et Cosmochimica Acta

www.elsevier.com/locate/gca

Simple models for disequilibrium fractional melting and batch melting with application to REE fractionation in abyssal peridotites

Yan Liang *, Boda Liu

Department of Earth, Environmental and Planetary Sciences, Brown University, Providence, RI 02912, United States

Received 13 May 2015; accepted in revised form 15 October 2015; Available online 10 November 2015

Abstract

Disequilibrium melting arises when the kinetics of chemical exchange between a residual mineral and partial melt is sluggish compare to the rate of melting. To better understand the role of a finite crystal–melt exchange rate on trace element fractionation during mantle melting, we have developed a disequilibrium melting model for partial melting in an upwelling steady-state column. We use linear kinetics to approximate crystal–melt mass exchange rate and obtain simple analytical solutions for cases of perfect fractional melting and batch melting. A key parameter determining the extent of chemical disequilibrium during partial melting is an element specific dimensionless ratio (ε) defined as the melting rate relative to the solid–melt chemical exchange rate for the trace element of interest. In the case of diffusion in mineral limited chemical exchange, ε is inversely proportional to diffusivity of the element of interest. Disequilibrium melting is important for the trace element when ε is comparable to or greater than the bulk solid–melt partition coefficient for the trace element (k). The disequilibrium fractional melting model is reduced to the equilibrium perfect fractional melting model when ε is much smaller than k. Hence highly incompatible trace elements with smaller mobilities in minerals are more susceptible to disequilibrium melting than moderately incompatible and compatible trace elements. Effect of chemical disequilibrium is to hinder the extent of fractionation between residual solid and partial melt, making the residual solid less depleted and the accumulated melt more depleted in incompatible trace element abundances relative the case of equilibrium melting.

Application of the disequilibrium fractional melting model to REE and Y abundances in clinopyroxene in abyssal peridotites from the Central Indian Ridge and the Vema Lithospheric Section, Mid-Atlantic Ridge revealed a positive correlation between the disequilibrium parameter ε and the degree of melting, which can be explained by an increase in melting rate and a decrease in REE diffusion rate in the upper part of the melting column. Small extent of disequilibrium melting for LREE and equilibrium melting for HREE in the upper part of the melting column can explain the elevated LREE abundances or spoon-shaped REE patterns in clinopyroxene in more refractory abyssal peridotites. The latter has often been attributed to melt refertilization.

1. INTRODUCTION

The distribution and fractionation of trace element between minerals and coexisting melt are important to the interpretation of mantle melting and melt migration processes. Interpretation of the trace elements in mantle rocks is based largely on simple melting models such as batch melting, fractional melting, dynamic or continuous melting,

* Corresponding author. Tel.: +1 401 863 9477.
E-mail address: Yan_Liang@brown.edu (Y. Liang).

http://dx.doi.org/10.1016/j.gca.2015.10.020
0016-7037/

and flux melting models (e.g., Shaw, 2006 and references therein). These simple models are also referred to as equilibrium melting models because residual solid and coexisting melt are in instantaneous chemical equilibrium during melting and melt migration. When the rate of chemical exchange between a residual mineral and partial melt is smaller than the rate of melting, chemical disequilibrium arises. Incomplete chemical exchange between interiors of mineral grains and their surrounding melt results in lesser extent of fractionation between residual solid and partial melt when compared to equivalent cases of equilibrium melting.

Models for trace element fractionation during disequilibrium mantle melting were presented in a number of studies (e.g., Allègre and Minster, 1978; Prinzhofer and Allègre, 1985; Iwamori, 1992, 1993; Qin, 1992; Van Orman et al., 2002; Liang, 2003a; Rudge et al., 2011). The earlier model of Allègre and Minster (1978) and Prinzhofer and Allègre (1985) assumes no chemical exchange between interiors of residual minerals and their surrounding melt. This is a case of complete disequilibrium melting that may be more relevant to melting under crustal (and hydrous) conditions where temperature is low and kinetics is sluggish. In a more general case of disequilibrium melting, melt and residual minerals exchange at finite rates compared to the rate of melting. A common treatment of disequilibrium melting is to consider grain-scale diffusive exchange between residual minerals and their surrounding melt during melting (Iwamori, 1992, 1993; Qin, 1992; Van Orman et al., 2002). This is a moving boundary problem that has no analytical solution. Although numerical solutions to the grain-scale moving boundary problem are straightforward, they become a formidable computational task at larger length scales and higher spatial dimensions. For large-scale geochemical mass transfer problems, such as melt generation beneath mid-ocean ridge spreading center, it is convenient and practical to reformulate the grain-scale mass transfer problem on continuum length scale where mineral and melt compositions are defined in a representative elementary volume (REV) that is much larger than mineral grain size through proper averaging and upscaling (e.g., Bear and Bachmat, 1990; Quintard and Whitaker, 1996; Whitaker, 1999). A simple treatment of grain-scale kinetics is to approximate diffusive flux at the mineral–melt interface by linear kinetics and uses an average rate constant to characterize mineral–melt diffusive exchange within the REV. This boundary layer approximation for solid–melt mass transfer in porous media has been widely used in studies of chemical chromatography and mantle metasomatism (e.g., Vermeulen, 1953; Glueckauf, 1955; Navon and Stolper, 1987; Bodinier et al., 1990; Cussler, 1997; Liang, 2003b). Using linear kinetics for mineral–melt diffusive exchange, Liang (2003a) generalized the dynamic melting model of McKenzie (1985, see also Albarède, 1995; Zou, 1998; Shaw, 2000) by assuming constant porosity in the solid and melt mass conservation equations and solved the system of coupled ordinary differential equations numerically following the temperature–pressure path of a subducting slab. Rudge et al. (2011) discussed continuum scale formulations for disequilibrium melting of a multi-component mantle from perspectives of non-equilibrium thermodynamics. Their expressions for mineral–melt mass transfer are essentially the same as those discussed in Liang (2003a,b) based on grain-scale averaging.

With the exception of the complete disequilibrium melting models of Allègre and Minster (1978) and Prinzhofer and Allègre (1985), there is no analytical solution for disequilibrium melting. The main purpose of the present study is to develop simple models for trace element fractionation during disequilibrium fractional melting and batch melting. Fractional melting and batch melting are two limiting styles of mantle melting. Melting in a one-dimensional steady-state upwelling column without instantaneous melt extraction is equivalent to batch melting (Ribe, 1985; Asimow and Stolper, 1999). The very depleted nature of incompatible trace elements in abyssal peridotites, olivine-hosted melt inclusions, and cumulates crystallized from basalts suggests that melting in the oceanic mantle is fractional or near fractional (e.g., Johnson et al., 1990; Johnson and Dick, 1992; Ross and Elthon, 1993; Sobolev and Shimizu, 1993; Shimizu, 1998). Fractional or near fractional melting requires efficient isolation of partial melt from residual solid. This can be achieved physically by channelized melt migration and chemically by disequilibrium melting and melt transport (Spiegelman and Kenyon, 1992; Hart, 1993; Kelemen et al., 1997). In the next section, we first outline a steady-state model for non-modal disequilibrium melting in an upwelling melting column. We then focus on a simplified problem of disequilibrium perfect fractional melting and present analytical solutions for a trace element in the partial melt and residual solid (Section 2). (Approximate solutions for near equilibrium batch melting are summarized in Appendices B and C.) We discuss key features of disequilibrium fractional melting and show that small extent of chemical disequilibrium can have a significant effect on the abundance and distribution of highly incompatible trace elements in residual solid (Section 3). As an example of geological application, we invert for degree of melting and a disequilibrium parameter that measures the extent of chemical disequilibrium from abundances of REE and Y in clinopyroxene in abyssal peridotites using the disequilibrium fractional melting model (Section 4). We assess effects of disequilibrium batch melting in the lower part of the melting column, melt refertilization in the upper most part of the melting column, and mantle metasomatism on REE patterns in clinopyroxene and discuss physical meanings of the inverted parameters (Section 5). Small extent of chemical disequilibrium may be present during adiabatic melting of the oceanic mantle.

2. DISEQUILIBRIUM MELTING MODELS

2.1. Model setup

We consider melting and melt migration in a one-dimensional steady-state upwelling column in which part of the melt generated is extracted to nearby channels or conduits. We are interested in steady-state distributions of a trace element in the interstitial melt (concentration C_f), residual bulk solid (C_s) and minerals (C_s^j, $j = 1, 2, \ldots, N$)

in the upwelling column when the system is locally out of chemical equilibrium, where N is the number of minerals in the system. For simplicity, we neglect diffusion and dispersion in the melt and use linear kinetics to approximate crystal–melt finite exchange that arises from diffusion in minerals and/or dissolution–reprecipitation (Navon and Stolper, 1987; Richter and DaPaolo, 1987; Bodinier et al., 1990; Liang, 2003b), viz.,

$$\{\text{crystal–melt exchange}\}_j = \rho_s \phi_j R_j (C_s^j - k_j C_f), \quad (1)$$

where ρ_s is the density of solid; ϕ_j is the volume fraction of mineral j in the system; R_j is the exchange rate constant for the trace element of interest between mineral j and the melt; k_j is the mineral j and melt partition coefficient for the trace element. (Notations are listed in Table 1.) Mass conservation equations for a non-radioactive trace element in the interstitial melt, residual solid, and a given mineral can be derived by considering advection, melting, and solid–melt mass exchange in a REV. The steady-state mass conservation equations are summarized in Appendix A (Eqs. (A1a)–(A1c)) and take on the common form

$$\{\text{mass flux}\}\frac{dC}{dz} = \{\text{melting}\} + \{\text{solid–melt exchange}\}, \quad (2)$$

where z is the vertical coordinate measured upward from the onset of melting ($z = 0$); C is the concentration of the trace element in the melt, bulk solid, or residual mineral. Eq. (2) can also be written in terms of the degree of melting experienced by the residual solid (F), as both the mass flux and z are functions of F (Eqs. (A3a)–(A3c) in Appendix A). The resulting equations are nonlinear (Eqs. (A4a)–(A4c)) and do not have exact solutions. To pinpoint the role of chemical disequilibrium in simple melting models, we seek analytical solutions to a simplified problem of disequilibrium melting in which mineral–melt exchange rates are the same for all the minerals in the systems, i.e., $R_1 = R_2 = \cdots = R_N = R$. Mass conservation equations for the simplified problem are

$$\varepsilon F(1-\mathbb{R})\frac{dC_f}{dF} = \varepsilon(C_s^p - C_f) + (C_s - kC_f), \quad (3a)$$

$$\varepsilon(1-F)\frac{dC_s}{dF} = \varepsilon(C_s - C_s^p) - (C_s - kC_f), \quad (3b)$$

$$\varepsilon(1-F)\frac{dC_s^j}{dF} = -(C_s^j - k_j C_f), \quad (3c)$$

where $\mathbb{R}$ is the dimensionless melt suction rate, defined as the fraction of melt removed from the residual solid (to a nearby channel) relative to the amount of melt produced by melting (Iwamori, 1994; Liang and Peng, 2010); C_s^p is the net concentration of solid that participates in the melting reaction (defined by Eq. (A1e) in Appendix A). For modal melting, we have $C_s = C_s^p$. ε is a (dimensionless) disequilibrium parameter, defined as the ratio between the bulk melting rate (Γ, in kg m^{-3} s^{-1}) and the mineral–melt exchange rate (R, in s^{-1}) for the element of interest, viz.,

$$\varepsilon = \frac{\Gamma}{\rho_s(1-\phi_f)R}. \quad (3d)$$

Table 1
List of key symbols used in the main text.

Symbol	Description
C_f	Concentration of a trace element in the instantaneous melt
C_f^{batch}	Instantaneous melt derived from the disequilibrium batch melting model
$\bar{C}_f$	Concentration of a trace element in the aggregated melt
C_s	Concentration of a trace element in the bulk solid
C_s^0	Concentration of the bulk solid at the onset of melting
C_s^j	Concentration of a trace element in mineral j
C_s^p	Net concentration of the solid participated in the melting reaction, Eq. (A1e)
D	Diffusion coefficient
d	Mineral grain size
F	Degree of melting experienced by the bulk solid
F_x	Degree of melting at which the melt compositions are the same between the equilibrium and disequilibrium melting models, Eq. (8)
f_p	Degree of melting at the onset of dynamic melting, Eq. (10c)
k	Bulk solid–melt partition coefficient
k_0	Bulk solid–melt partition coefficient at the onset of melting
k_e	Effective bulk solid–melt partition coefficient defined by Eq. (7)
k_p	Bulk solid–melt partition coefficient for the melting reaction
p_j	Weight fraction of mineral j participated in the melting reaction
R	Mineral–melt exchange rate constant, subscript j refers to mineral j
V_f, V_s	Velocity of the melt or solid
V_s^0	Solid upwelling rate at the onset of melting
w_j	Weight fraction of mineral j in the solid
z	Vertical coordinate, measured from the base of the melting column
α	Ratio between the melt and solid mass or mass flux ratio, Eq. (10b) or (10d)
ε	Element specific disequilibrium parameter, Eq. (3d), subscript j refers to mineral j
ε_{La}, ε_{REE}	Disequilibrium parameter for La or REE
ϕ_f, ϕ_j	Volume fraction of the melt or mineral j
Γ	Melting rate of the bulk solid
ρ_f, ρ_s	Density of melt or solid
$\mathbb{R}$	Dimensionless melt suction rate, $0 \leqslant \mathbb{R} \leqslant 1$

The bulk solid–melt partition coefficient k varies during non-modal melting and takes on the usual expression

$$k = \frac{k_0 - k_p F}{1 - F}, \quad (3e)$$

where k_0 is the bulk partition coefficient at the onset of melting ($F = 0$) and k_p is the partition coefficient calculated according to melting reaction. Eqs. (3a)–(3c) are closed by the following boundary conditions at the bottom of the melting column:

$$C_f(0) = \frac{\varepsilon k_p + k_0}{\varepsilon + k_0}\frac{C_s^0}{k_0}, \quad C_s(0) = C_s^0, \quad C_s^j(0) = \frac{k_j}{k_0}C_s^0, \quad (3f, 3g, 3h)$$

where the boundary condition for the melt is obtained by setting $F = 0$ in Eq. (3a).

Given solid–melt partition coefficients, the steady-state disequilibrium melting model described by Eqs. (3a)–(3h) has three dimensionless parameters: degree of melting (F), melt suction rate ($\mathbb{R}$), and disequilibrium parameter (ε). For a fixed melting rate, $\varepsilon \propto 1/R$ and hence goes to zero when mineral–melt exchange coefficient R is very large. Eqs. (3a)–(3h) then recover the limit of equilibrium melting. In the absence of melt extraction or suction along the melting column, i.e., regions of the upwelling mantle far away from channels ($\mathbb{R} = 0$), Eqs. (3a)–(3h) form a complete model for disequilibrium batch melting. Approximate solutions to a case of near equilibrium batch melting (i.e., when $\varepsilon \ll 1$) are presented in Appendix B. In the limit of complete and instantaneous melt extraction along the melting column ($\mathbb{R} = 1$), we have the case of perfect fractional melting. Eqs. (3a)–(3h) then have exact solutions which we will detail below.

2.2. Disequilibrium fractional melting model

During perfect fractional melting, any melt generated in the melting column is instantaneously removed from residual solid, leaving no porosity in the upwelling melting column, viz., $\mathbb{R} = 1$. The net concentration of solid participated in the melting reaction, C_s^p, is related to the bulk solid concentration through the simple relation, $C_s^p/C_s = k_p/k$. From Eq. (3a), we have a simple relation for the melt and bulk solid compositions during fractional melting,

$$C_f = \frac{\varepsilon k_p + k}{\varepsilon + k}\frac{C_s}{k}. \tag{4}$$

Substituting Eq. (4) into Eq. (3b) and upon integration, we have exact solutions for the case of non-modal disequilibrium perfect fractional melting,

$$C_f = \frac{\varepsilon k_p + k}{\varepsilon + k}\frac{C_s^0}{k_0}\left[1 - \frac{\varepsilon + k_p}{\varepsilon + k_0}F\right]^{\frac{1-k_p}{\varepsilon + k_p}}, \tag{5a}$$

$$C_s = \frac{kC_s^0}{k_0}\left[1 - \frac{\varepsilon + k_p}{\varepsilon + k_0}F\right]^{\frac{1-k_p}{\varepsilon + k_p}}, \tag{5b}$$

$$C_s^j = \frac{k_j}{k}C_s = \frac{k_j C_s^0}{k_0}\left[1 - \frac{\varepsilon + k_p}{\varepsilon + k_0}F\right]^{\frac{1-k_p}{\varepsilon + k_p}}. \tag{5c}$$

The average or aggregated melt composition is given by the global mass conservation equation

$$\bar{C}_f = \frac{1}{F}[C_s^0 - (1-F)C_s]. \tag{5d}$$

The analytical solutions Eqs. (5a)–(5d) are simplified to the non-modal equilibrium perfect fraction melting model when $\varepsilon = 0$. These equations are reduced to the case of complete disequilibrium melting when ε is much greater than the larger of 1 and k_p. The melt and residual bulk solid compositions are given by the simple expressions

$$C_f = \frac{k_p}{k_0}C_s^0 \quad \text{and} \quad C_s = \frac{k}{k_0}C_s^0, \tag{6a, 6b}$$

which are equivalent to Eqs. (6) and (7) in Prinzhofer and Allègre (1985). Hence melt and residual solid compositions are different from the starting solid composition during non-modal complete disequilibrium melting, as noted in earlier studies (Prinzhofer and Allègre, 1985; Van Orman et al. 2002). Examples calculated using Eqs. (5a) and (5b) and a comparison with the dynamic or continuous melting model will be presented in the next section.

3. GENERAL FEATURES OF DISEQUILIBRIUM FRACTIONAL MELTING

To obtain simple analytical solutions, we assumed that the mineral–melt exchange rate constant R_j is the same for all the minerals in the melting column. In terms of diffusive mass transfer through mineral grains, this assumption implies that zoning profiles for the trace element of interest in minerals are the same for all the minerals in the system when normalized to grain sizes and rim concentrations. Consequently, (average) concentrations of the trace element in the minerals are proportional to each other, i.e., according to their partition coefficients (cf. Eq. (5c)), although chemical equilibrium has not been established. In a more general case when the exchange rates are different among the minerals, the simple relation given by Eq. (5c) may not be valid. (We will come back to this point in Section 5.1.) With this caveat in mind, we now examine the main features of the disequilibrium fractional melting below.

3.1. Hindered fractionation and an effective partitioning coefficient

Eq. (4) allows us to define an effective or apparent bulk partition coefficient, k_e, for fractional melting,

$$k_e = \frac{C_s}{C_f} = \frac{\varepsilon + k}{\varepsilon k_p + k}k, \tag{7}$$

which varies between k and k/k_p for equilibrium fractional melting and complete disequilibrium melting, respectively. The effective partition coefficient k_e is a constant for modal melting, but varies as a function of F for non-modal melting. Since $k_e > k$ for incompatible elements, the effect of chemical disequilibrium is to hinder the extent of fractionation between the solid and the melt, making the residual solid less depleted and the accumulated melt more depleted relative the case of equilibrium melting. (The opposite is true for a compatible trace element.) This is illustrated in Figs. 1a and 1c for an incompatible trace element ($k_0 = k_p = 0.025$) and several choices of ε. Interestingly, abundances of the incompatible trace element in the instantaneous melt are higher than the case of equilibrium fractional melting at higher degrees of melting, i.e., there is a cross over between the dashed line (equilibrium melting) and the solid lines (disequilibrium melting) in Fig. 1b. The cross over arises because residual solid is less fractionated and hence has higher incompatible trace element abundances during disequilibrium melting (Fig. 1a). For the case of modal melting (i.e., $k_p = k_0$), an explicit

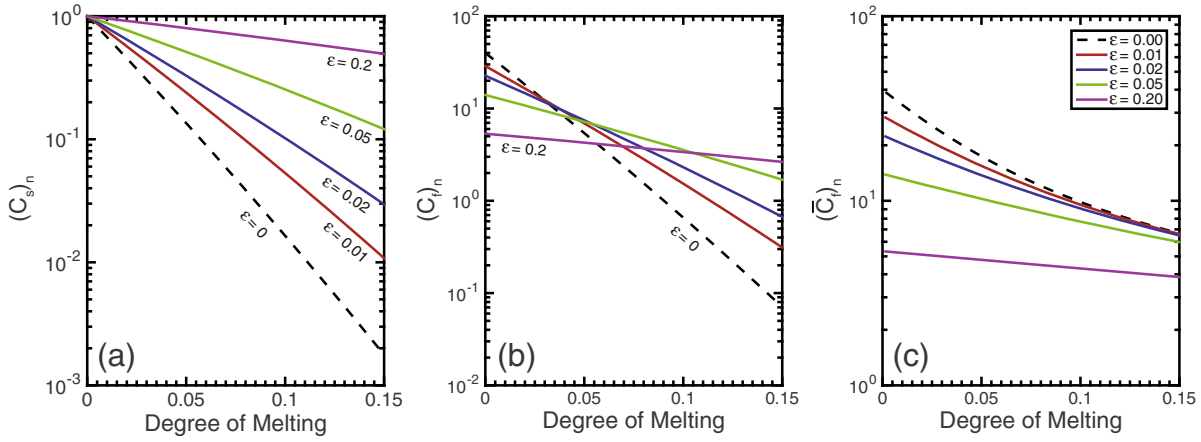

Fig. 1. Variations of an incompatible trace element ($k_0 = k_p = 0.025$) in residual solid, panel (a), instantaneous melt, panel (b), and aggregated melt, panel (c), as a function of the degree of melting for 5 selected disequilibrium parameter ε. Concentrations are normalized by initial solid concentration at the onset of melting. The case of equilibrium fractional melting is shown as dashed lines.

expression for the degree of melting at the cross over, F_x, can be obtained,

$$F_x = 1 - \left[k_0\left(\frac{\varepsilon+1}{\varepsilon+k_0}\right)\right]^{\frac{k_0}{\varepsilon}\frac{\varepsilon+k_0}{1-k_0}}, \quad (8)$$

where the term in parenthesis is the reciprocal of the effective partition coefficient. Fig. 2 displays the strong dependence of F_x on the bulk partition coefficient. For melting of a spinel lherzolite mantle, the cross over F_x is 7–10% for Yb, 1–3% for La, and 0.3–0.5% for U and Th for $\varepsilon = 0.01$–0.2, according to the bulk partition coefficients listed in Workman and Hart (2005). For moderately incompatible and compatible trace elements ($k_0 > 0.4$), F_x is greater than 30% and hence unlikely to occur during lherzolite melting. Hence disequilibrium fractional melting is less effective in depleting highly incompatible trace element abundances in instantaneous melt than equilibrium fractional melting when $F > F_x$.

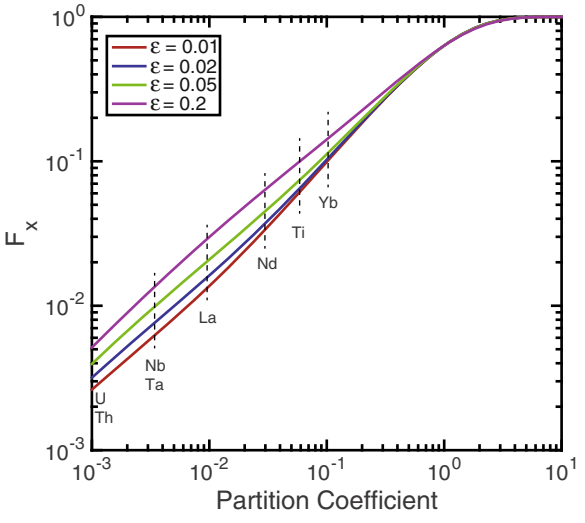

Fig. 2. Variations of the degree of melting at the cross over (F_x) as a function of bulk solid–melt partition coefficient for 4 choices of the disequilibrium parameter ε. Partition coefficients of selected incompatible trace elements are shown as vertical dashed lines (partitioning data from Workman and Hart, 2005). See text for discussion.

Figs. 1a and 3 demonstrate that even small extent of chemical disequilibrium can have a significant effect on the abundance and relative fractionation of highly incompatible trace elements ($k_0 < 0.01$) in residual solid. The highly incompatible trace element enriched patterns are similar to those produced by equilibrium fractional melting of an enriched source. This mild enrichment is due to the term $\varepsilon + k_p$ in the disequilibrium melting model (Eq. (5b)). For elements with $k_p < \varepsilon$, their ability to fractionate among each other is masked by ε. When $k_p \ll \varepsilon$, abundance of the incompatible trace element in residual solid is independent of its partition coefficient and takes on the asymptotic value,

$$C_s = \frac{k}{k_0} C_s^0 (1-F)^{\frac{1}{\varepsilon}}. \quad (9)$$

This is an important feature of disequilibrium fractional melting. Ratios of the highly incompatible trace element abundances in the residual solid then are the same as those in the source region during modal melting, independent of the extent of melting. This is illustrated by the sub-horizontal lines in the upper left corner of Fig. 3 for a case of modal melting.

3.2. Comparison with continuous melting and steady-state melting models

In terms of mathematic expression, solutions to the disequilibrium fractional melting model (Eqs. (5a) and (5b)) are very similar to those to the dynamic or continuous melting models. The continuous melting model consists of two parts: an early batch melting (up to $F = f_p$) and a second stage "dynamic melting" whereby a constant and (usually) small fraction of melt (ϕ_f) is retained in the residual solid (e.g., Zou, 1998; Shaw, 2006). According to the models of Albarède (1995), Zou (1998), and Shaw (2000), the melt

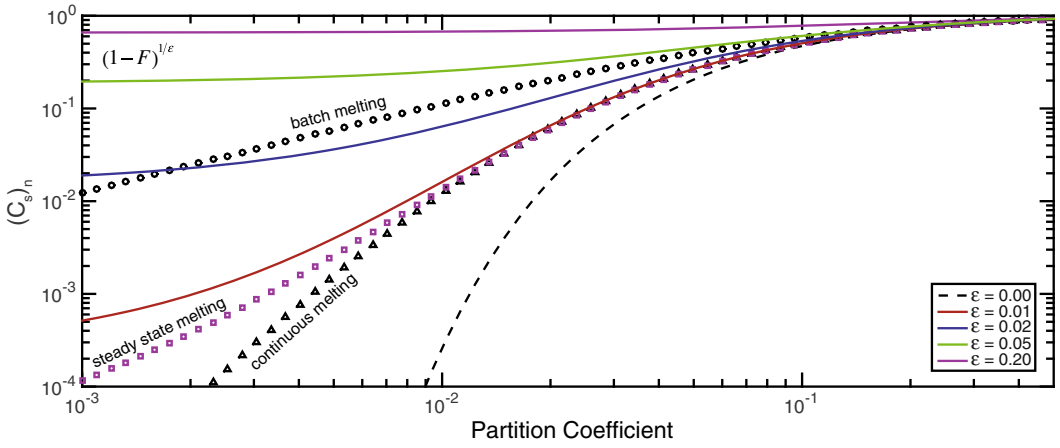

Fig. 3. Variations of the normalized residual solid compositions as a function of bulk solid–melt partition coefficient for 5 choices of the disequilibrium parameter ε and at 8% melting. For comparison, compositions in residual solid produced by equilibrium batch melting (circles), steady-state melting (diamonds, $\mathbb{R} = 0.75$), and continuous melting (triangles, $\alpha = 0.01$) models are also shown. The case of $\varepsilon = 0$ corresponds to equilibrium perfect fractional melting (dashed line). See text for discussion.

composition (C_f^{dyn}) for the second stage dynamic melting ($F > f_p$) is given by the equation

$$C_f^{dyn} = \frac{C_s^0}{k_0 + (1-k_p)f_p}\left[\frac{\alpha + k_0 - (\alpha + k_p)F}{\alpha + k_0 - (\alpha + k_p)f_p}\right]^{\frac{1-k_p}{\alpha + k_p}}, \quad (10a)$$

$$\alpha = \frac{\rho_f \phi_f}{\rho_s(1-\phi_f)}, \quad f_p = \frac{\alpha}{1+\alpha}, \quad (10b, 10c)$$

where α is the mass ratio between coexisting melt and solid; f_p is the degree of melting experienced by the solid matrix at the onset of dynamic melting. The continuous melting model is obtained under the assumption of no relative flow or motion between interstitial melt and residual solid. In the context of steady state melting in an upwelling column, one can obtain an expression for the melt composition that is identical to Eq. (10a) by redefining the parameter α as the ratio between the melt mass flux and the solid mass flux (Liang, 2008),

$$\alpha = \frac{\rho_f \phi_f V_f}{\rho_s(1-\phi_f)V_s}. \quad (10d)$$

For small degree of batch melting ($f_p \ll 1$), Eq. (10a) can be simplified by expanding the denominator in the square bracket in a Taylor series. Retaining the first order, we have

$$C_f^{dyn} = \frac{\alpha\gamma + 1}{\alpha + k_0} C_s^0 \left[1 - \frac{\alpha + k_p}{\alpha + k_0} F\right]^{\frac{1-k_p}{\alpha + k_p}}, \quad (11a)$$

where γ is defined as

$$\gamma = \frac{1}{k_0 + (1-k_p)f_p}. \quad (11b)$$

We can now make direct comparison between the continuous melting model and the disequilibrium fractional melting model. The case of $\alpha = \varepsilon$ is most interesting because terms associated with the square bracket in Eqs. (5a) and (11a) are equivalent. Differences between the two models then arise from the remaining terms in the two equations. For simplicity, we consider the case $k_p = k_0$ (i.e., modal melting). For an incompatible element, $\gamma > 1$. Hence for the same degree of melting F, the incompatible trace element abundance in the melt calculated using the continuous melting model (Eq. (11a)) will be higher than that derived from the disequilibrium fractional melting model (Eq. (5a)). The opposite is true for the solid. When $k_0 \gg f_p$, $\gamma \sim 1/k_0$ and the concentration of the trace element in the residual solid derived from the dynamic melting model (C_s^{dyn}) is indistinguishable from that from the disequilibrium fractional melting, viz.,

$$C_s^{dyn} = \frac{k}{k_0} C_s^0 \left[1 - \frac{\alpha + k_p}{\alpha + k_0} F\right]^{\frac{1-k_p}{\alpha + k_p}}. \quad (12)$$

These are illustrated in Fig. 3 for the case of $\alpha = 0.01$ (open triangle), $\varepsilon = 0.01$ (solid red line), and $F = 8\%$. Hence in terms of numerical values the two models are equivalent except for trace elements having bulk partition coefficients significantly less than the value of ε or α.

The disequilibrium fractional melting model (Eqs. (5a) and (5b)) also bears resemblance to the steady-state melting models of Iwamori (1994), Ozawa (2001), and Liang and Peng (2010) which take on the simple form,

$$C_f^{ss} = \frac{C_s^0}{k_0}\left[1 - \frac{k_p + \mathbb{R} - 1}{k_0} F\right]^{\frac{1-k_p}{k_p + \mathbb{R} - 1}}, \quad (13)$$

where C_f^{ss} is the abundance of the trace element in the melt according to the steady-state model. Note the subtle difference in the exponent: $\mathbb{R} - 1 \leqslant 0$ in Eq. (13) but $\varepsilon \geqslant 0$ in the disequilibrium fractional melting model (Eq. (5a)). With proper choice of the melt suction rate, concentrations of moderately incompatible elements calculated using the steady-state melting model are practically the same as those obtained using the disequilibrium fractional melting model or the continuous melting model. The mismatches are, again, in the highly incompatible trace elements (Fig. 3, $\mathbb{R} = 0.75$).

Hence one cannot distinguish disequilibrium fractional melting from equilibrium near fractional melting based on moderately incompatible trace element abundances in residual solid unless the extent of chemical disequilibrium is large (i.e., when $\varepsilon > k$).

3.3. Element specific disequilibrium parameter ε

The most important difference among the three melting models is in the physical meaning of the melting parameters α, $\mathbb{R}$, and ε. Here α in the continuous melting model is the melt-to-solid mass or mass flux ratio (Eq. (10b) or (10d)), while $\mathbb{R}$ in the steady-state melting model is the melt suction rate relative to the melting rate. Both are physical parameters common to all the elements in the system. In contrast, ε in the disequilibrium melting model is the melting rate relative to the solid–melt chemical exchange rate (Eq. (3d)) and therefore is specific to the element of interest. For diffusion in solid limited mass transfer, the exchange rate R is proportional to diffusion coefficient of the element of interest in the mineral (D), viz.,

$$R = \frac{3\beta D}{d^2}, \tag{14}$$

where d is the average or effective mineral grain size; β is a geometric factor. $\beta = 1$, 4, or 5 for diffusion in a plane sheet, a cylinder or a sphere (e.g., Navon and Stolper, 1987; Bodinier et al., 1990; Liang, 2003b). Hence ε is inversely proportional to the diffusion coefficient.

Van Orman et al. (2001) demonstrated that diffusion of REE in diopside depend strongly on their ionic radii. Fig. 4 displays the disequilibrium parameter ε_{REE} for REE in clinopyroxene (cpx) for 5 choices of the disequilibrium parameter ε_{La} for La. Here we scale ε_{REE} for REE to that of La using the reciprocal relationship (cf. Eq. (14)),

$$\varepsilon_{REE} = \frac{D_{La}}{D_{REE}}\varepsilon_{La}, \tag{15}$$

where D_{REE} are the diffusion coefficients for trivalent REE in cpx at 1300 °C and 1 GPa, calculated using the diffusion data in Van Orman et al. (2002). The disequilibrium parameter ε_{REE} decreases by a factor of 20 from La to Lu for a given ε_{La}.

The significance of element specific ε_{REE} is demonstrated by the variations in the light and heavy REE abundances in residual cpx for a case of non-modal melting of spinel lherzolite in Fig. 5a–d ($F = 6\%$, 10%, 14%, and 18%). For 0–18% non-modal melting of the lherzolite, the bulk partition coefficient of La (k_{La}) decreases from 0.0096 to 0.003, while the bulk partition coefficient of Lu (k_{Lu}) decreases from 0.13 to 0.066. For the ranges of disequilibrium parameter considered (Fig. 4), we have $\varepsilon_{La} > k_{La}$ and $\varepsilon_{Lu} \leqslant k_{Lu}$. Hence disequilibrium fractional melting has a significant effect on the light REE (LREE) in residual cpx but a small to negligible effect on the heavy REE (HREE) in cpx. This is in contrast to the case of constant ε for REE where middle to heavy REE are also fractionated through the term $\varepsilon + k$ in Eq. (5c) (see Supplementary Fig. S1 for an example of $F = 10\%$ and $\varepsilon_{REE} = \varepsilon_{La}$). At higher degrees of melting, LREE abundances in cpx are very sensitive to the extent of chemical disequilibrium, whereas middle to heavy REE in cpx become progressively depleted in response to melting. Disequilibrium melting for LREE and (near) equilibrium melting for HREE result in "spoon-shaped" LREE enriched patterns (Fig. 5c and d) which have often been attributed to shallow level melt refertilization (see Section 5.2 for discussion). It is important to note that the LREE enrichment in this case is not due to an enriched mantle source, but rather the depletion of middle to heavy REE at higher degrees of melting. This is an important feature of disequilibrium fractional melting.

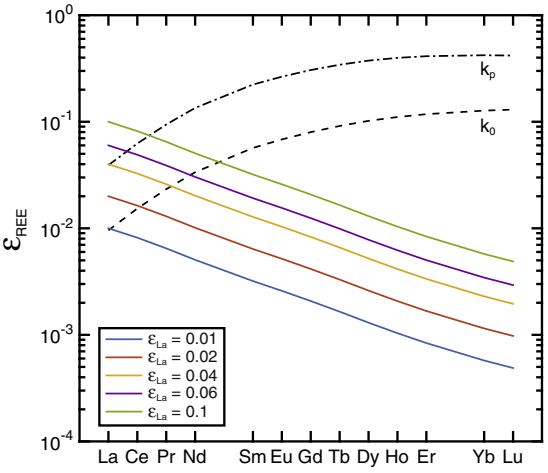

Fig. 4. Variations of the disequilibrium parameter for REE (ε_{REE}) for 5 choices of ε_{La}. Here ε_{REE} are calculated using Eq. (15) and diffusion coefficients for trivalent REE in diopside at 1300 °C and 1 GPa from the diffusion data in Van Orman et al. (2002). Partition coefficients (k_0 and k_p) for non-modal melting of a spinel lherzolite are also shown.

Given the simple analytical solutions obtained in this study, it is possible to assess the extent of chemical disequilibrium experienced in residual peridotites by inverting the disequilibrium parameter ε_{La} and the extent of melting F from abundances of REE in residual peridotites. We consider two such examples in the next section.

4. REE AND Y DEPLETION IN ABYSSAL PERIDOTITES

The abundance of REE in cpx in abyssal peridotites has often been used to infer the degree of melting and style of melt extraction in the oceanic mantle (e.g., Johnson et al., 1990; Johnson and Dick, 1992; Dick and Natland, 1996; Niu and Hèkinian, 1997; Hellebrand et al., 2002; Hellebrand and Snow, 2003; Niu, 2004; Brunelli et al., 2006, 2014; Seyler et al., 2007; Liang and Peng, 2010). Interpretations of the trace element data in previous studies are based on equilibrium melting models. An important conclusion from these studies is that melting beneath the mid-ocean spreading center is fractional or near fractional. In a recent study, Liang and Peng (2010) inverted melting parameters (F and $\mathbb{R}$) from REE and Y abundances in cpx in abyssal peridotites from three localities along the Central Indian Ridge (CIR, data reported by Hellebrand et al., 2002) using the steady-state melting model Eq. (13)

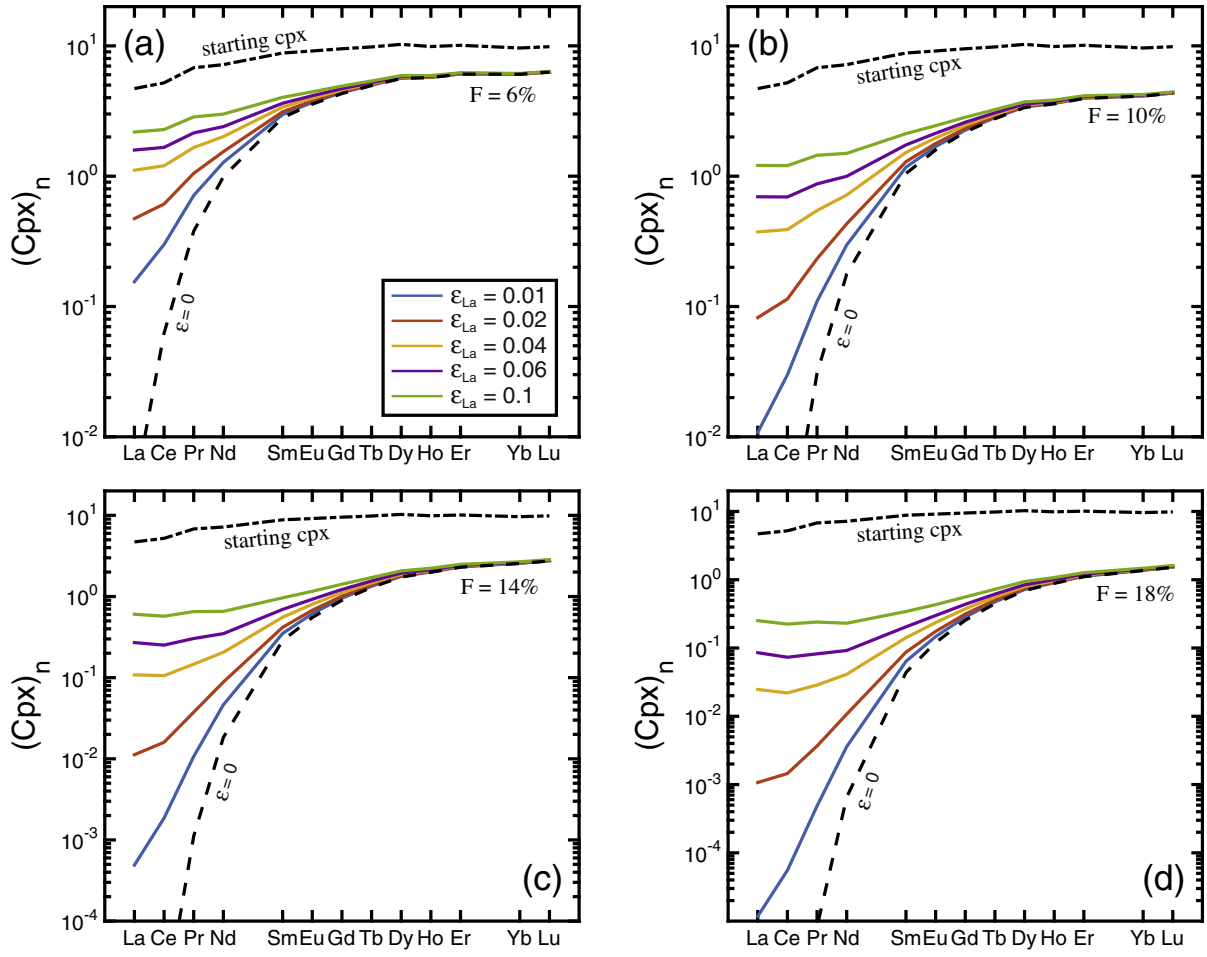

Fig. 5. Variations of REE abundances in residual clinopyroxene (normalized to CI chondrite) during disequilibrium fractional melting of a spinel lherzolite. For reference, REE abundances in clinopyroxene at the onset of melting are shown as dash-dotted lines. The cases of equilibrium fractional melting are shown as dashed lines ($\varepsilon = 0$).

and its modified forms that include batch melting in the lower part of the melting column and melting initiated in the garnet stability field. Of the 22 cpx data reported by Hellebrand et al. (2002), they were only able to obtain satisfactory fits to 10 LREE depleted samples using Eq. (13) or its modified forms. An interesting question is if REE patterns in the remaining 12 samples can be explained by the disequilibrium fractional melting model. A broader question is if disequilibrium melting is important to mantle melting beneath the mid-ocean ridge spreading center.

To address these questions, we first invert the melting parameters (F and ε_{La}) from REE + Y abundances in the 22 cpx samples from CIR using the disequilibrium fractional melting model presented in this study. (Disequilibrium parameters for Y and other REE are related to ε_{La} via Eq. (15).) We then expand our database by including 35 cpx data from the Vema Lithospheric Section (VLS), Mid-Atlantic Ridge (Brunelli et al., 2006). Peridotites from these two studies are free of plagioclase and generally depleted in incompatible trace element abundances. Major element abundances in minerals in these samples exhibit systematic variations that are consistent with melting trends (Hellebrand et al., 2001, 2002; Brunelli et al., 2006; Cipriani et al., 2009). Additionally, $^{143}Nd/^{144}Nd$ isotope ratios in cpx from 14 of the 35 VLS samples were measured by Cipriani et al. (2004), which allows us to assess the role of mantle source heterogeneity in the data interpretation. In order to use the simple melting models, we make the following assumptions: (1) REE + Y abundances in cpx from these two studies represent residues of mantle melting and that melting initiates in the spinel lherzolite field; (2) trace element abundances in the starting mantle are homogeneous and the same as the average DMM (Workman and Hart, 2005); and (3) solid–melt chemical exchange for REE is rate limited by diffusion in cpx. Sun and Liang (2014) showed that the elevated HREE abundances in cpx in abyssal peridotites can be attributed to subsolidus redistribution of REE between cpx and orthopyroxene and melting in the garnet stability field is not required to explain the observed REE patterns in residual cpx. Assumptions (1) and (2) imply that REE + Y abundances in cpx are not affected by other magmatic processes such as refertilization or metasomatism. We will come back to this point in Section 5.2.

We invert for melting parameters F and ε_{La} for a given set of REE + Y data in residual cpx using Eq. (5c) and a nonlinear least squares regression method (Liang and Peng, 2010). We scale ε_{REE} for Y and other REE to ε_{La} according to Eq. (15) using the diopside diffusion data in Van Orman et al. (2002) at 1300 °C and 1 GPa. Diffusion coefficients of trivalent cations not listed in Van Orman et al. (2002) are interpolated according to ionic radii of REE^{3+}. We use the average pyroxene–melt and olivine–melt REE partition coefficients along the 1300 °C mantle adiabat for the DMM starting composition (Sun and Liang, 2012; Yao et al., 2012; Sun and Liang, 2014) and the melting reaction for spinel lherzolite of Kinzler and Grove (1992) to calculate bulk partition coefficients k_0 and k_p in Eq. (5c) (Fig. 4). To compare with equilibrium melting models, we also invert melting parameters for the steady-state melting model (F and $\mathbb{R}$) and the continuous melting model (F and α), when possible. La abundances in 2 CIR and 6 VLS samples are too high (chondrite normalized La/Ce > 2) to be consistent with any melting model starting with the average DMM. Melting parameters for these samples were obtained by excluding La in the nonlinear least squares regression analyses. Eleven of the 12 CIR samples that were excluded in the study of Liang and Peng (2010) can now be fitted by the disequilibrium fractional melting model. The exception is sample CIRCE93-7, which has a "humped" or middle REE enriched pattern and cannot be fitted by any of the melting models (Supplementary Fig. S2). One sample (S2209-1) from VLS is also excluded from this study because of fewer elements available for this sample (which results in none convergence in our least squares inversion). Best estimates of the melting parameters for the 56 samples are listed in Supplementary Tables S1 and S2. Nonlinear least squares fits to individual samples using the three melting models are presented in Supplementary Figs. S2 and S3. Below we summarize the main results.

Fig. 6a presents our best estimates of the melting parameters (ε_{La} and F) for the 21 CIR samples (circles) and 35 VLS samples (triangles). Figs. 7a–c display examples of measured REE patterns along with nonlinear least squares fits to the observed data using the disequilibrium fractional melting model (solid line). The disequilibrium parameter ε_{La} ranges from effectively 0 to 0.036 and F from 5% to 21%, defining a broad positive correlation in Fig. 6a. According to their REE patterns, the 56 cpx data can be divided into two groups: those with $\varepsilon_{La} < 0.02$ and those with $\varepsilon_{La} > 0.02$. The former includes all the samples with LREE depleted patterns (Fig.7a, 30 VLS samples and 11 CIR samples), while the latter consists of 13 samples with variable La and Ce enrichment (Fig.7b and c), 4 from VLS and 10 from CIR. REE patterns in cpx in the small ε_{La} group can also be explained by the two equilibrium melting models, whereas REE patterns in cpx in the larger ε_{La} group can only be explained by the disequilibrium melting model (Supplementary Fig. S2 and S3).

The Cr# in spinel is a useful proxy for the degree of melting (Hellebrand et al., 2001). For the CIR and VLS samples, the Cr# in spinel is negatively correlated with Yb, Na_2O, and TiO_2 abundances in residual cpx. Figs. 8a and 8b compare our inverted ε_{La} and F with the Cr# in spinel in the same peridotite samples. The broad positive correlations between the spinel Cr# and the inverted F for the two sets of data further confirm the conclusions of Hellebrand et al. (2002) and Brunelli et al. (2006, see also Cipriani et al., 2009) that middle and heavy REE abundances in these samples were largely controlled by mantle melting. Interestingly, our inverted ε_{La} are only weakly correlated with the Cr# in spinel.

5. FURTHER DISCUSSION

5.1. The assumption of $R_1 = R_2 = \cdots = R_N$

The simple analytical solutions (Eqs. (5a)–(5c)) were obtained under the assumption that the mineral–melt exchange rate constants are the same for all the minerals in the residue. According to Cherniak and Liang (2007), REE diffusion in enstatite is not sensitive to ionic radius

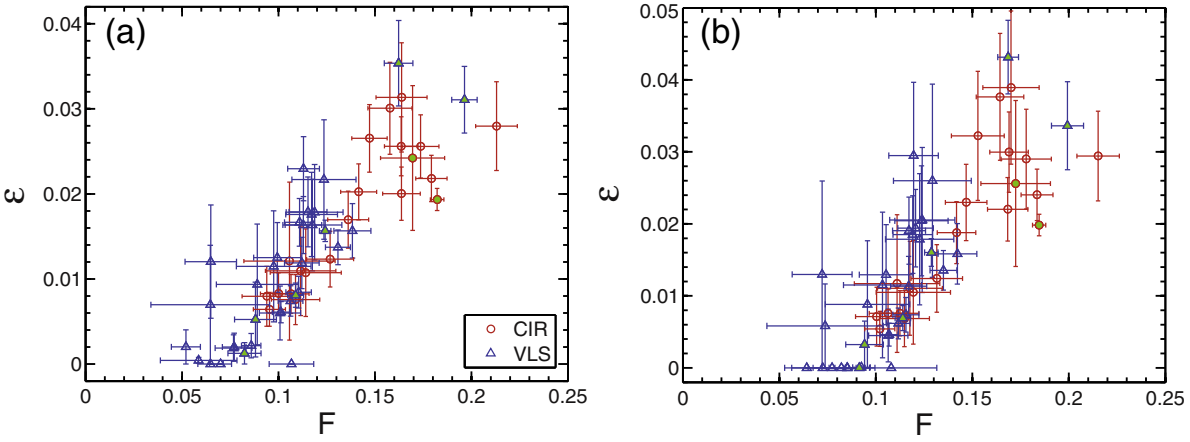

Fig. 6. Correlations between the inverted disequilibrium parameter ε_{La} and the degree of melting F for the 56 abyssal peridotite samples included in this study. (a) Parameters obtained using the disequilibrium fractional melting model; (b) parameters obtained using the disequilibrium batch-fractional melting model. Here we assume 4% batch melting in the lower part of the melting column and ε_{La} for batch melting is half that for fractional melting. The error bars are ±1 standard deviations. Filled symbols represent samples with $(La/Ce)_N > 2$.

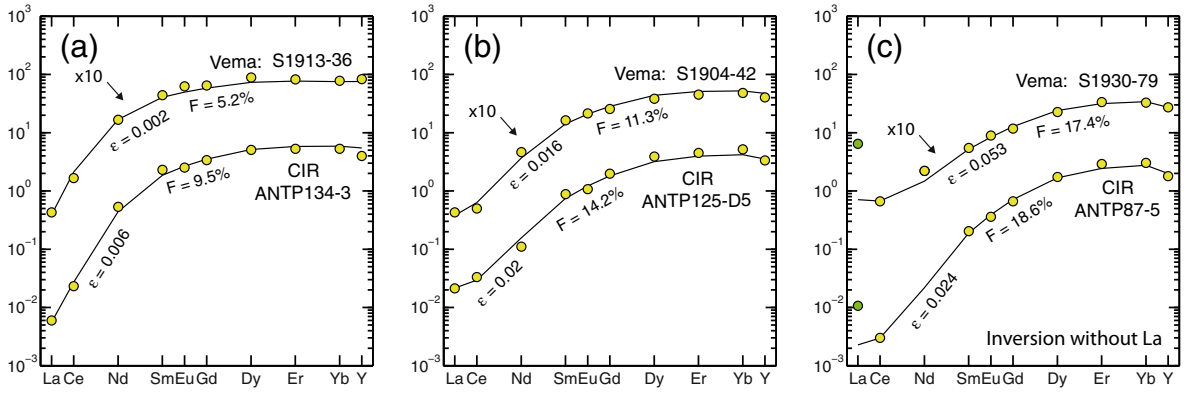

Fig. 7. Plots showing nonlinear least squares fits (solid lines) to selected REE and Y data (symbols) in clinopyroxene in abyssal peridotites from the Central Indian Ridge reported by Hellebrand et al. (2002) and the Vema Lithospheric Section, Mid-Atlantic Ridge report by Brunelli et al. (2006). For clarity, data from VLS were elevated by a factor of 10. (a) LREE depleted samples; (b) Mild LREE enriched samples; (c) examples with $(La/Ce)_N > 2$ and their La abundances were excluded in the inversion (green circles). Initial mineral proportions in the starting spinel lherzolite are 53% olivine, 27% orthopyroxene (opx), 17% clinopyroxene (cpx), and 3% spinel. The melting reaction is from Kinzler and Grove (1992). Compositions of starting mantle are the average DMM reported by Workman and Hart (2005). Pyroxene–melt and olivine–melt partition coefficients are average values for melting along the 1300 °C mantle adiabat for the DMM starting composition (Sun and Liang, 2012, 2014; Yao et al., 2012). The spinel-melt partition coefficients are from Kelemen et al. (2003). REE and Y abundances in clinopyroxene were normalized to CI chondrite using the values of Anders and Grevesse (1989). (For interpretation of the references to colour in this figure legend, the reader is referred to the web version of this article.)

and their diffusivities are comparable to those of Gd and Dy in diopside (Van Orman et al., 2001). To assess the effect of REE diffusion in orthopyroxene (opx) on the inverted melting parameters, we solved the more general mass conservation Eqs. (A4a)–(A4c) in Appendix A numerically using diffusion data reported in Van Orman et al. (2002) for cpx and Cherniak and Liang (2007) for opx. We set the degree of melting to 10% and ran simulations for a range of disequilibrium parameter ε_{La} in cpx that are comparable to those obtained from our inversion (10^{-4} to 0.04, Fig. 6a). We then invert the numerically generated REE patterns in cpx for ε_{La} and F using the simplified disequilibrium fractional melting model (Eq. (5c)). We found that values of the inverted ε_{La} and F are within 10% and 3% of the input values, respectively. This excellent agreement is due to the small values of ε_{La} ($\leqslant 0.04$) used in the simulation (i.e., melting is near equilibrium for HREE and slight disequilibrium for LREE) and the considerably smaller LREE partition coefficients in opx. The latter limits the contribution of opx to the overall LREE budget. As illustrated in Fig. 5, LREE abundances in residual cpx are more sensitive to small values of ε_{La} than HREE. Hence the simple melting model presented in this study (Eqs. (5a)–(5c)) is especially suitable for studying near equilibrium fractional melting of spinel peridotite.

5.2. Disequilibrium batch melting

It has long been recognized that geochemical interpretations of fractional or near-fractional melting are not unique. Ribe (1985) showed that steady-state melting in a one-dimensional upwelling melting column without melt extraction to nearby channels is equivalent to batch melting. Kelemen et al. (1997) demonstrated that the depleted LREE patterns in cpx in abyssal peridotites can be explained equally well by a hybrid model involving a combination of batch melting and fractional melting. Asimow (1999) argued that fractional melting alone is not capable of explaining the systematic variations in major element in abyssal peridotites and that a combination of batch melting and fractional melting similar to that proposed by Kelemen et al. (1997) can explain the variations in both the major and trace elements in abyssal peridotites [see also Niu et al. (1997) for an alternative explanation]. Liang and Peng (2010) showed that 5% equilibrium batch melting followed by 10–15% equilibrium near fractional melting can also explain the 10 LREE depleted cpx samples of Hellebrand et al. (2002) from CIR. It is likely that both fractional melting and batch melting have played important roles in magma generation beneath the mid-ocean ridges.

We can construct a steady-state melting model similar to that of Kelemen et al. (1997) and Asimow (1999) by considering disequilibrium batch melting in the lower part of the melting column (up to $F = f_p$, Appendix B) and disequilibrium fractional melting in the upper part of the melting column (Appendix C). This disequilibrium batch-fractional melting model has two additional parameters (f_p and ε) to account for batch melting in the lower part of the melting column. Since (equilibrium) batch melting results in considerably less incompatible trace element fractionation than fractional melting (Fig. 4) and disequilibrium batch melting further reduces such fractionation (Appendix B), disequilibrium batch-fractional melting is capable of producing the mildly LREE enriched and spoon-shaped REE patterns in cpx in residual peridotites (for an example, see Supplementary Fig. S5). Fig. 6b presents the inverted ε_{La} and F at $f_p = 4\%$ for the 56 CIR and VLS samples. Since temperatures in the lower part of the melting column are higher than those in the upper region during adiabatic melting, ε_{La} for batch melting is likely smaller than that for fractional melting in the upper part of the melting column (see Section 5.4 for additional discussion). For purpose of

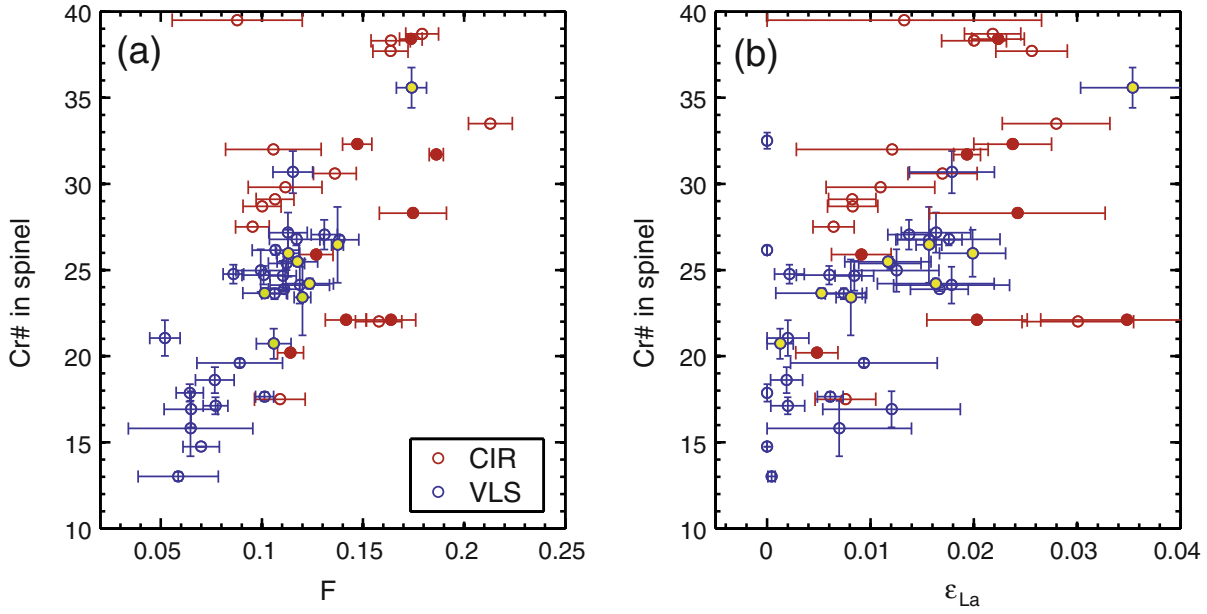

Fig. 8. Correlations between the Cr# in spinel and the inverted degree of melting F (panel a) or the disequilibrium parameter ε_{La} (b) for the 56 abyssal peridotite samples included in this study. The error bars are ±1 standard deviations. Filled symbols represent samples with $(La/Ce)_N > 2$.

demonstration, here we assume that ε_{La} for batch melting is half the size of ε_{La} for fractional melting in the melting column. The disequilibrium parameter ε_{La} for fractional melting ranges from 0 to 0.042 and F from 6% to 21%, which are very similar to the case shown in Fig. 6a for perfect fractional melting. The slightly larger ε_{La} for samples experienced higher degree of melting ($F > 14\%$) in Fig. 6b is due to disequilibrium batch melting in the lower part of the melting column. The preceding exercise further demonstrates the importance of batch melting in the lower part of the upwelling column to the interpretation of the observed REE data in abyssal peridotites. Indeed, both linear stability analysis and numerical simulations of reactive porous flow have shown that it is difficult to form high-porosity channels in the lower part of an upwelling melting column in the absence of chemical heterogeneity (e.g., Spiegelman and Kelemen, 2003; Hewitt, 2010; Hesses et al., 2011; Liang et al., 2010, 2011; Weatherley and Katz, 2012). In the absence of high-porosity channels, batch melting in the framework of Ribe (1985) is likely the dominant mode of melt generation during decompression melting.

5.3. Refertilization and mantle metasomatism

Shallow level refertilization of refractory harzburgite by basalts formed in the lower part of the melting column has been widely believed to play an important role in the formation of plagioclase-bearing abyssal peridotites and in producing variably LREE enriched patterns in plagioclase-free peridotites (e.g., Dick, 1989; Cannat et al., 1992; Elthon, 1992; Girardeau and Francheteau, 1993; Niu and Hèkinian, 1997; Seyler and Bonatti, 1997; Seyler et al., 2001; Tartarotti et al., 2002; Niu, 2004; Takazawa et al., 2007; Godard et al., 2008; Brunelli and Seyler, 2010; Müntener et al., 2010; Warren and Shimizu, 2010). Both Hellebrand et al. (2002) and Brunelli et al. (2006) presented textural evidences for small amount of trapped and crystallized melt in the peridotite samples they studied (see also Seyler et al., 2001). Hellebrand et al. (2002) showed that the hump-shaped REE pattern in sample CIRCE93-7 can be explained by a mixing model that involves a refractory harzburgite or lherzolite and a slightly less depleted instantaneous melt produced by 13% and 12% continuous melting with 0.5% trapped melt (see their Fig. 9). Brunelli et al. (2006) further expanded the refertilization model of Hellebrand et al. (2002) by considering various refertilizing melt compositions (instantaneous melt, quasi-instantaneous melt, and partially aggregated melt extracted over a range of depth in the melting column). According to their model, melting started in the garnet stability field and refertilization with 0.1–0.8% of partially aggregated melt could explain REE abundances in 31 of the 35 VLS samples (see their Table 8 and Fig. 12). They noted that "the amount of melting in the garnet stability field is higher than expected for a slow-spreading scenario as in the VLS". The melting and refertilization model of Brunelli et al. (2006) has six parameters: degrees of melting in the garnet and spinel stability fields, residual porosity, refertilizing melt composition and melt fraction, and proportion of cpx crystallized from the refertilizing melt. Trace element modeling with such large number of parameters often suffers from nonlinear trade-off among the parameters, resulting in non-unique solutions to the melting-refertilization problem (e.g., Niu and Hèkinian, 1997; Niu, 2004). For example, we can also produce variably LREE enriched patterns in cpx by mixing small degree melts derived from melting of a spinel lherzolite with a refractory harzburgite.

It is not clear physically how refertilization by small degree melts takes place in an upwelling mantle.

Hellebrand et al. (2002) noted that Na_2O content in some of the CIR samples are too high to be consistent with a melting trend and attributed it to refertilization at shallow depth (see also Elthon, 1992). Fig. 9a displays variations of Na_2O in cpx as a function of our inverted ε_{La} for the 56 CIR and VLS samples. In general, Na_2O contents in cpx from CIR are higher than those from VLS at a given ε_{La} or F, suggesting the melting condition or source composition may be different between the two regions. However, there is no obvious correlation between ε_{La} and Na_2O in cpx for samples with $\varepsilon_{La} > 0.02$. Interestingly, samples with Na_2O in cpx > 0.5 wt% have lower ε_{La} values (<0.013, Fig. 9a), whereas samples with the highest ε_{La} have the lowest Na_2O in cpx.

Metasomatism by a melt or fluid derived from a heterogeneous mantle source can also give rise to elevated LREE patterns in peridotites. Eight samples (2 from CIR and 6 from VLS) included in this study have higher La abundances that cannot be explained by any melting models. Fig. 9b shows that there is no correlation between $(La/Ce)_N$ and the disequilibrium parameter ε_{La}. Hence, a process that gives rise to La enrichment in cpx is unlikely responsible for the higher ε_{La} derived from the more refractory (high F) samples. Peridotite samples that experienced mantle metasomatism often possess enriched isotope signatures. Cipriani et al. (2004) reported Sr and Nd isotopes of cpx mineral separates for 14 of the 35 samples included in the study of Brunelli et al. (2006). Fig. 10 displays variations of our inverted ε_{La} with the 14 $^{143}Nd/^{144}Nd$ data. The data are somewhat scatter and can be interpreted in two ways: (1) there is a weak negative correlation between ε_{La} and $^{143}Nd/^{144}Nd$ if one excludes the most isotopically depleted sample; (2) ε_{La} and $^{143}Nd/^{144}Nd$ in 9 of the 14 samples enclosed in the dashed box in Fig. 10 are essentially uncorrelated. For example, for the small range of $^{143}Nd/^{144}Nd$ within the hatched region in Fig. 10, ε_{La} varies from 0 to 0.016. Presently, there is no Nd isotope

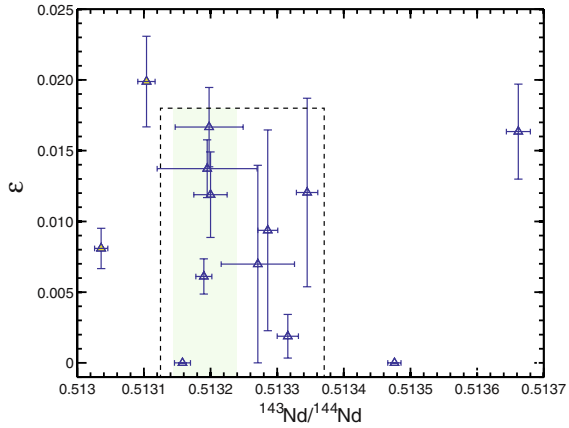

Fig. 10. Correlations between the inverted disequilibrium parameter ε_{La} and $^{143}Nd/^{144}Nd$ ratio in clinopyroxene in the abyssal peridotite samples from the Vema Lithospheric Section, Mid-Atlantic Ridge report by Brunelli et al. (2006). Isotope data are from Cipriani et al. (2004). The two boxes are drawn to facilitate discussion.

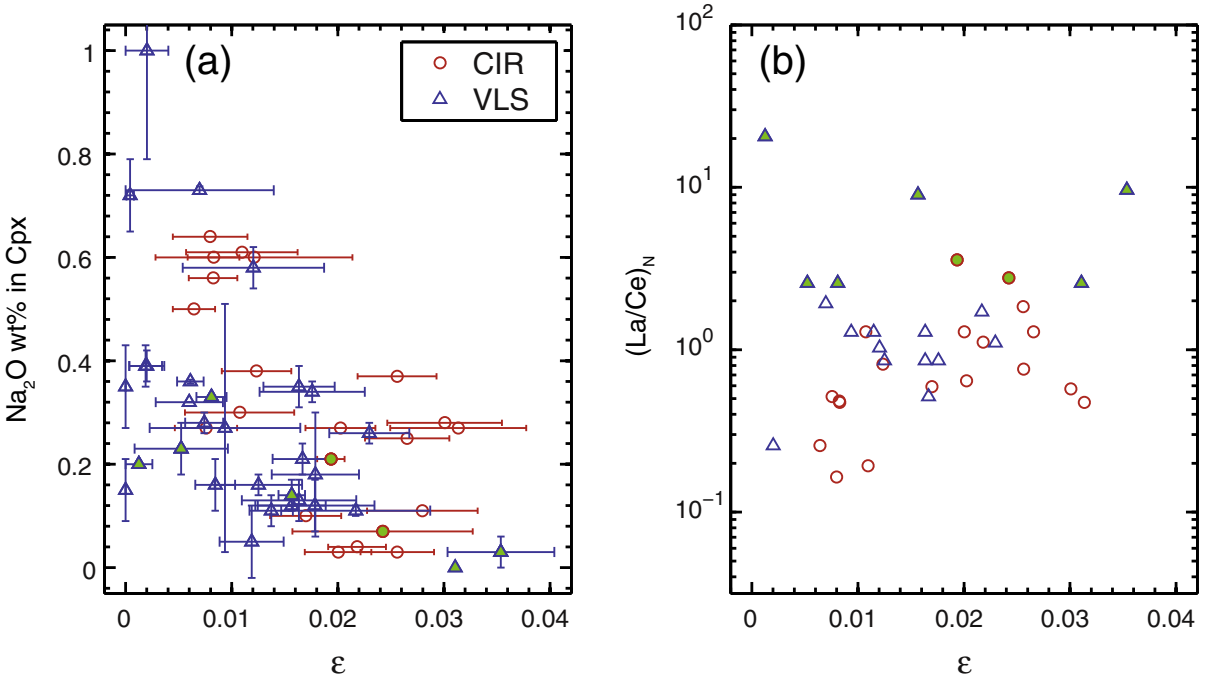

Fig. 9. Correlations between the inverted disequilibrium parameter ε_{La} and Na_2O (panel a) or $(La/Ce)_N$ (panel b) in clinopyroxene for the 56 abyssal peridotite samples included in this study. The error bars are ±1 standard deviations. Filled symbols represent samples with $(La/Ce)_N > 2$.

data for samples with $\varepsilon_{La} > 0.02$. Based on a larger dataset (21 samples), Cipriani et al. (2004) showed that there is a broad negative correlation between Cr# in spinel and $^{143}Nd/^{144}Nd$ ratio in cpx in the VLS samples ($r^2 = 0.60$, see their Fig. 4, although additional isotope data for the VLS samples indicate that the correlation, if any, is weaker than that shown in their Fig. 4, Dr. Daniele Brunelli personal communication, 2015). However, given the weak positive correlation between Cr# in spinel and ε_{La} in Fig. 8b, we cannot rule out the second interpretation. Finally, it is interesting to note that the most isotopically enriched sample in Fig. 10 has the highest $(La/Ce)_N$ ratio (20) but low ε_{La} (0.008 ± 0.0015). Hence the limited data considered here cannot establish an obvious link between mantle metasomatism and samples with higher ε_{La} values (>0.02). More isotope data are needed to further assess the relationship between metasomatism and disequilibrium melting in abyssal peridotites.

5.4. Disequilibrium melting and the positive correlation between F and ε_{La}

The melting parameters obtained in this study also depend on starting mantle composition, modal abundance, and stoichiometric coefficients in the melting reaction. (This statement also applies to other melting models.) For example, we can fit the same REE pattern in residual cpx with a smaller degree of melting if we decrease cpx abundance in the starting mantle. However, the positive correlation between ε_{La} and F remains and hence is a robust feature of the two data sets. This illustrated in Supplementary Fig. S4 for a starting mantle with 13% cpx.

The association of larger disequilibrium parameter ε_{La} with higher degree of melting F in the HREE depleted samples (Figs. 6a and 6b) is intriguing and demands further examination. Although nonlinear trade-off from least squares inversion of the REE + Y data can give rise to a positive correlation between ε_{La} and F, variations of ε_{La} and F due to such aliasing are small and cannot explain the larger ranges shown in Fig. 6. Within the framework of adiabatic melting in an upwelling homogeneous mantle column, a simple explanation of the positive correlations in Fig. 6 is an increase in melting rate and a decrease in diffusive exchange rate in the upper part of the melting column (cf. Eqs. (3d) and (14)). The melting rate (Γ) is related to the upwelling rate (V_s) and melt productivity (dF/dz) through Eq. (A2c) in Appendix A, viz.,

$$\Gamma = \frac{\rho_s(1-\phi_f)V_s}{1-F}\frac{dF}{dz}. \tag{16}$$

From Eqs. (3d) and (14), we have a simple expression for the disequilibrium parameter

$$\varepsilon = \frac{V_s d^2}{3\beta(1-F)D}\frac{dF}{dz}. \tag{17}$$

Diffusivities of LREE in cpx decrease by a factor of 10 or so during adiabatic mantle melting (which results in a decrease in temperature). Asimow et al. (1997, 2001) demonstrated through thermodynamic calculations that the melt productivity or melting rate increases significantly at lower pressures during adiabatic fractional melting of lherzolite and cpx-bearing harzburgite. Fig. 11a shows the increase of melting rate along the 1310 °C mantle adiabat for two choices of upwelling rate (15 and 30 mm/yr, red and blue solid lines, respectively). Here the melting rates are derived from pMELTS (Ghiorso et al., 2002) for near fractional melting of DMM. Fig. 11b displays the positive correlation between ε_{La} and F along the 1310 °C mantle adiabat, calculated using Eq. (17) with the La diffusion coefficient from Van Orman et al. (2002) for a constant cpx grain size of 1 mm and two choices of upwelling rate (solid lines). The cpx grain size likely decreases during mantle melting, although the details are unknown. Fig. 11b displays two additional examples calculated by assuming cpx

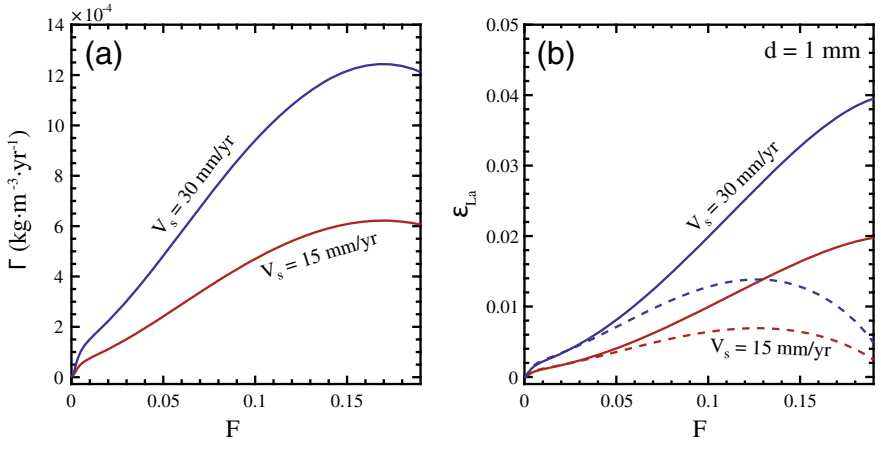

Fig. 11. Variations of the calculated melting rate (a) and disequilibrium parameter ε_{La} (b) along an adiabatic near-fractional melting path for two choices of upwelling rates: 15 mm/yr (blue solid and dashed lines) and 30 mm/yr (red solid and dashed lines). Two cases of clinopyroxene grain size are considered in (b): constant grain size (1 mm, solid lines) and decreasing grain size (dashed lines). The melt productivity for the anhydrous DMM is derived from a near-fractional melting calculation from pMELTS (Ghiorso et al., 2002). La diffusivity in clinopyroxene is from Van Orman et al. (2002). For simplicity, we assume a spherical grain shape ($\beta = 5$ in Eq. (16)). See text for discussion. (For interpretation of the references to colour in this figure legend, the reader is referred to the web version of this article.)

grain size proportional to its modal abundance during melting (red and blue dashed lines for upwelling rates of 15 and 30 mm/yr, respectively). The decrease of ε_{La} at higher F (>13%) is due to a significant reduction in cpx grain size, which outweighs the increase in melt productivity. Given the large uncertainties in cpx grain size, grain shape, and grain size distribution, a more realistic case may be the one that is bracketed by the solid and dashed lines in Fig. 11b, which defines a broad positive correlation between ε_{La} and F, similar to that observed in abyssal peridotites (Fig. 6). The preceding examples highlight the importance of grain size and upwelling rate in controlling ε in the disequilibrium melting model.

The small values of ε_{La} and the positive correlation between ε_{La} and F (Fig. 6) suggest that melting in the low half of the melting column ($F < 14\%$) can be treated as near equilibrium melting for all the REE in residual cpx and that melting in the entire melting column can be treated as equilibrium melting for HREE in cpx. Indeed, REE patterns in cpx in moderately depleted samples and HREE in all but one sample (CIRCE93-7) from the two regions can also be explained by equilibrium near fractional melting models. Small extent of chemical disequilibrium persists for LREE in more refractory harzburgites. This may be a common phenomenon for abyssal peridotites and possibly residual peridotites from other tectonic settings where melting rate is high and kinetics is sluggish (e.g., slab melting and hydrous melting in mantle wedge). Given the relatively fast rates of diffusive exchange of major elements in mantle minerals compared to REE diffusion in pyroxenes, results from this study imply that disequilibrium melting is unlikely to play a major role in the fractionation of major and compatible trace elements during adiabatic melting in the oceanic mantle. Although we cannot rule out shallow level refertilization as a mechanism for LREE enrichment in cpx from CIR and VLS samples, we note that refertilization is not required by the disequilibrium fractional and batch-fractional melting models. It is likely that both disequilibrium melting and shallow level refertilization have played important roles in the fractionation of LREE and other highly incompatible trace elements in at least some of the abyssal peridotites. More petrologic and geochemical studies are needed to distinguish samples affected by refertilization from samples experienced disequilibrium melting. Highly incompatible trace elements with smaller mobility, such as LREE, Nb, Ta, U and Th, are especially useful in deciphering the extent of chemical disequilibrium between residual solid and partial melt during decompression mantle melting.

ACKNOWLEDGMENTS

YL wishes to thank Frank Richter for many simulating discussion regarding disequilibrium melting during the 1991–1992 academic year at the University of Chicago where solutions similar to the near equilibrium batch melting model outlined in Appendix B were first obtained. We thank Soumen Mallick for pointing out the existing isotope data for the VLS samples and for useful discussion. This paper benefited from thoughtful review comments from Daniele Brunelli, Eric Hellebrand, and Richard Katz. This work was supported by NSF grant OCE-1156706.

APPENDIX A. GOVERNING EQUATIONS

We consider a general problem of trace element fractionation during disequilibrium melting and melt migration in a one-dimensional steady-state upwelling column in which part of the melt generated is extracted to nearby channels or conduits. At steady state, mass conservation equations for a non-radioactive trace element in the interstitial melt, residual solid, and a given mineral take the forms

$$\rho_f \phi_f V_f \frac{dC_f}{dz} = (C_s^p - C_f)\Gamma + \rho_s(1-\phi_f)\sum_{j=1}^{N} w_j R_j (C_s^j - k_j C_f), \tag{A1a}$$

$$\rho_f(1-\phi_f)V_s \frac{dC_s}{dz} = (C_s - C_s^p)\Gamma - \rho_s(1-\phi_f)\sum_{j=1}^{N} w_j R_j (C_s^j - k_j C_f), \tag{A1b}$$

$$\rho_s \phi_j V_s \frac{dC_s^j}{dz} = -\rho_s \phi_j R_j (C_s^j - k_j C_f), \tag{A1c}$$

$$C_s = \sum_{j=1}^{N} w_j C_s^j, \quad C_s^p = \sum_{j=1}^{N} p_j C_s^j, \tag{A1d, A1e}$$

where ρ is the density; ϕ_f is the porosity; V is the velocity; Γ is the bulk solid melting rate; w_j is the weight fraction of mineral j in residual solid; R_j is the exchange rate constant for the trace element of interest between mineral j and the melt; k_j is the mineral j and melt partition coefficient for the trace element. The subscripts or superscripts f and s refer to properties of the melt and solid, respectively. The left-hand side (LHS) of Eqs. (A1a)–(A1c) is due to advection of the melt or the solid. The first terms on the right-hand side (RHS) of Eqs. (A1a), (A1b) account for non-modal melting of the solid (the melting term in Eq. (A1c) is eliminated by mass conservation constraint of the mineral), while the second terms are due to solid–melt mass transfer in response to diffusion in minerals and/or dissolution–reprecipitation. These RHS terms are very similar to those given in Liang (2003a) for a disequilibrium dynamic melting model. Summation of Eq. (A1c) over all the minerals, while noting w_j varies during melting, recovers the bulk solid mass conservation Eq. (A1b).

For the steady-state upwelling melting column, the melt and solid mass fluxes on the LHS of Eqs. (A1a) and (A1b) are related to the degree of melting (F) experienced by the solid matrix (Liang and Peng, 2010), viz.,

$$\rho_f \phi_f V_f = \rho_s V_s^0 F(1-\mathbb{R}), \tag{A2a}$$

$$\rho_s(1-\phi_f)V_s = \rho_s V_s^0 (1-F), \tag{A2b}$$

$$V_s \frac{dF}{dz} = \frac{(1-F)\Gamma}{\rho_s(1-\phi_f)}, \tag{A2c}$$

where V_s^0 is the upwelling rate at the onset of melting ($z = 0$). Substituting Eqs. (A2a)–(A2c) into Eqs. (A1a)–(A1c), we obtain a set of mass conservation equations in terms of the degree of melting,

$$F(1-\mathbb{R})\Gamma\frac{dC_f}{dF}=(C_s^p-C_f)\Gamma+\rho_s(1-\phi_f)\sum_{j=1}^{N}w_jR_j(C_s^j-k_jC_f), \quad \text{(A3a)}$$

$$(1-F)\Gamma\frac{dC_s}{dF}=(C_s-C_s^p)\Gamma-\rho_s(1-\phi_f)\sum_{j=1}^{N}w_jR_j(C_s^j-k_jC_f), \quad \text{(A3b)}$$

$$(1-F)\Gamma\frac{dC_s^j}{dF}=-\rho_s(1-\phi_f)R_j(C_s^j-k_jC_f). \quad \text{(A3c)}$$

For constant melting rate, Eqs. (A3a)–(A3c) can be further simplified by dividing each equation by the product $\rho_s(1-\phi_f)R_1$,

$$\varepsilon_1F(1-\mathbb{R})\frac{dC_f}{dF}=\varepsilon(C_s^p-C_f)+\sum_{j=1}^{N}w_j\frac{R_j}{R_1}(C_s^j-k_jC_f), \quad \text{(A4a)}$$

$$\varepsilon_1(1-F)\frac{dC_s}{dF}=\varepsilon(C_s-C_s^p)-\sum_{j=1}^{N}w_j\frac{R_j}{R_1}(C_s^j-k_jC_f), \quad \text{(A4b)}$$

$$\varepsilon_1(1-F)\frac{dC_s^j}{dF}=-\frac{R_j}{R_1}(C_s^j-k_jC_f), \quad \text{(A4c)}$$

where the disequilibrium parameter ε_1 is defined with respect to the exchange rate constant for the element of interest in mineral 1, viz.,

$$\varepsilon_1=\frac{\Gamma}{\rho_s(1-\phi_f)R_1}. \quad \text{(A4d)}$$

When $R_1=R_2=\cdots=R_N=R$, Eqs. (A4a)–(A4d) reduce to Eqs. (3a)–(3d) which are the working model in this study.

APPENDIX B. A SIMPLE MODEL FOR NEAR EQUILIBRIUM BATCH MELTING

During batch melting ($\mathbb{R}=0$) the melt and bulk solid compositions at any point in the melting column are related to each other through total mass conservation (e.g., Ribe, 1985; Asimow and Stolper, 1999),

$$FC_f+(1-F)C_s=C_s^0, \quad \text{(B1)}$$

where C_s^0 is the concentration of the trace element in the bulk solid at the onset of melting. Exact solutions to Eqs. (3a)–(3h) are complicated, involving incomplete gamma functions. Given the main results from this study, here we seek approximate solutions for a case of near equilibrium batch melting, i.e., when $\varepsilon\ll 1$. The solutions can be obtained by expanding the melt and solid concentrations in terms of the small disequilibrium parameter ε using the regular perturbation method,

$$C_f=C_f^{(0)}+\varepsilon C_f^{(1)}+\varepsilon^2C_f^{(2)}+\cdots, \quad \text{(B2a)}$$

$$C_s=C_s^{(0)}+\varepsilon C_s^{(1)}+\varepsilon^2C_s^{(2)}+\cdots, \quad \text{(B2b)}$$

where numbers in parentheses in the superscript refer to zero-th order, first-order, and second-order solutions, respectively. The zero-th order solutions recover the equilibrium case, viz.,

$$C_f^{(0)}=\frac{C_s^0}{k_0+(1-k_p)F}, \quad \text{(B3a)}$$

$$C_s^{(0)}=\frac{kC_s^0}{k_0+(1-k_p)F}. \quad \text{(B3b)}$$

For near equilibrium batch melting, a first order correction is adequate. The approximate solutions to Eqs. (3a)–(3h) (for $\mathbb{R}=0$), accurate to the order of ε^2, are

$$C_f^{batch}=C_f^{(0)}\left\{1-\frac{(1-F)(1-k_p)(k_0-k_pF)}{[F+(1-F)k]^2}\varepsilon\right\}, \quad \text{(B4a)}$$

$$C_s^{batch}=C_s^{(0)}\left\{1+\frac{F(1-F)(1-k_p)}{[F+(1-F)k]^2}\varepsilon\right\}, \quad \text{(B4b)}$$

$$C_s^{j,batch}=\frac{k_j}{k}C_s^{batch}, \quad \text{(B4c)}$$

where k is the bulk partition coefficient (Eq. (3e)). Hence $C_s^{batch}>C_s^{(0)}$ and $C_f^{batch}<C_f^{(0)}$ for incompatible elements during batch melting.

APPENDIX C. A DISEQUILIBRIUM BATCH-FRACTIONAL MELTING MODEL

Here we consider a case of disequilibrium batch melting in the lower part of the melting column ($F\leqslant f_p$) and disequilibrium fractional melting in the upper part of the melting column. Solutions for a trace element in the melt, bulk solid, and mineral j in the upper part of the melting column can be readily derived given Eqs. (B4a)–(B4c) and take on the following expressions

$$C_f=C_f^{batch}\left[\frac{\varepsilon+k_{fp}}{\varepsilon k_p+k_{fp}}\right]\left[\frac{\varepsilon k_p+k}{\varepsilon+k}\right]\left[\frac{\varepsilon+k_0-(\varepsilon+k_p)F}{\varepsilon+k_0-(\varepsilon+k_p)f_p}\right]^{\frac{1-k_p}{\varepsilon+k_p}}, \quad \text{(C1a)}$$

$$C_s=\frac{k}{k_{fp}}C_s^{batch}\left[\frac{\varepsilon+k_0-(\varepsilon+k_p)F}{\varepsilon+k_0-(\varepsilon+k_p)f_p}\right]^{\frac{1-k_p}{\varepsilon+k_p}} \quad \text{(C1b)}$$

$$C_s^j=\frac{k_j}{k_{fp}}C_s^{batch}\left[\frac{\varepsilon+k_0-(\varepsilon+k_p)F}{\varepsilon+k_0-(\varepsilon+k_p)f_p}\right]^{\frac{1-k_p}{\varepsilon+k_p}}, \quad \text{(C1c)}$$

where k_{fp} is the bulk partition coefficient evaluated at $F=f_p$; k is the bulk partition coefficient evaluated at F; C_s^{batch} is from Eq. (B4b) with $F=f_p$. Solution for the aggregated melt is the same as Eq. (5d). Note the melt and solid concentrations are continuous across the boundary separating the two styles of melting (at $F=f_p$). The disequilibrium parameter ε may take on two different values in the batch and fractional melting parts of the upwelling column, as the melting rate and diffusion coefficient for the element of interest vary along the upwelling column during adiabatic melting.

APPENDIX D. SUPPLEMENTARY DATA

Supplementary data associated with this article can be found, in the online version, at http://dx.doi.org/10.1016/j.gca.2015.10.020.

REFERENCES

Anders E. and Grevesse N. (1989) Abundances of the elements: meteoritic and solar. *Geochim. Cosmochim. Acta* **53**, 197–214.

Albarède F. (1995) *Introduction to Geochemical Modeling*. Cambridge Univ. Press, New York.

Allègre C. J. and Minster J. F. (1978) Quantitative models of trace element behavior in magmatic processes. *Earth Planet. Sci. Lett.* **38**, 1–25.

Asimow P. D. (1999) A model that reconciles major- and trace-element data from abyssal peridotites. *Earth Planet. Sci. Lett.* **169**, 303–319.

Asimow P. D. and Stolper E. M. (1999) Steady-steady mantle–melt interactions in one dimension: I. Equilibrium transport and melt focusing. *J. Petrol.* **40**, 475–494.

Asimow P. D., Hirschmann M. M. and Stolper E. M. (1997) An analysis of variations in isentropic melt productivity. *Phil. Trans. R. Soc. Lond.* **A355**, 255–281.

Asimow P. D., Hirschmann M. M. and Stolper E. M. (2001) Calculation of peridotite partial melting from thermodynamic models of minerals and melts, IV. Adiabatic decompression and the composition and mean properties of mid-ocean ridge basalts. *J. Petrol.* **42**, 963–998.

Bear J. and Bachmat Y. (1990) *Introduction to Modeling of Transport Phenomena in Porous Media*. Kluwer Academic Publishers, Dordrecht.

Bodinier J. L., Vasseur G., Vernieres J., Dupuy C. and Fabries J. (1990) Mechanisms of mantle metasomatism: geochemical evidence from the Lherz orogenic peridotite. *J. Petrol.* **31**, 597–628.

Brunelli D. and Seyler M. (2010) Asthenospheric percolation of alkaline melts beneath the St. Paul region (Central Atlantic Ocean). *Earth Planet. Sci. Lett.* **289**, 393–405.

Brunelli D., Seyler M., Cipriani A., Ottolini L. and Bonatti E. (2006) Discontinuous melt extraction and weak refertilization of mantle peridotites at the Verma lithospheric section (Mid-Atlantic Ridge). *J. Petrol.* **47**, 745–771.

Brunelli D., Paganelli E. and Seyler M. (2014) Percolation of enriched melts during incremental open-system melting in the spinel field: a REE approach to abyssal peridotites from the Southwest Indian Ridge. *Geochim. Cosmochim. Acta* **127**, 190–203.

Cannat M., Bideau D. and Bougault H. (1992) Serpentinized peridotites and gabbros in the Mid-Atlantic Ridge axial valley at 15°37′N and 16°52′N. *Earth Planet. Sci. Lett.* **109**, 87–106.

Cherniak D. J. and Liang Y. (2007) Rare earth element diffusion in natural enstatite. *Geochim. Cosmochim. Acta* **71**, 1324–1340.

Cipriani A., Brueckner H. K., Bonatti E. and Brunelli D. (2004) Oceanic crust generated by elusive parents: Sr and Nd isotopes in basalt–peridotite pairs from Mid-Atlantic Ridge. *Geology* **32**, 657–660.

Cipriani A., Bonatti E., Brunelli D. and Ligi M. (2009) 26 million years of mantle upwelling below a segment of the Mid-Atlantic Ridge: the Vema Lithospheric Section revisited. *Earth Planet. Sci. Lett.* **285**, 87–95.

Cussler E. L. (1997) *Diffusion Mass Transfer in Fluid Systems*. Cambridge University Press, New York.

Dick H. J. B. (1989) Abyssal peridotites, very slow spreading ridges and ocean ridge magmatism, Saunders, A. D. and Norry, M. J. (eds.). *Magmatism in the Ocean Basins. Geological Society Special Publication* **42**, 71–105.

Dick H. H. B. and Natland J. H. (1996) Late-stage melt evolution and transport in the shallow mantle beneath the East Pacific Rise. *Proc. Ocean Drilling Program Sci. Results* **147**, 103–134.

Elthon D. (1992) Chemical trends in abyssal peridotites: refertilization of depleted suboceanic mantle. *J. Geophys. Res.* **97**, 9015–9025.

Ghiorso M. S., Hirschmann M. M., Reiners P. W. and Kress V. C. I. I. I. (2002) The pMELTS: an revision of MELTS aimed at improving calculation of phase relations and major element partitioning involved in partial melting of the mantle at pressures up to 3 GPa. *Geochem. Geophys. Geosyst.* **3**(5). http://dx.doi.org/10.1029/2001GC000217.

Girardeau J. and Francheteau J. (1993) Plagioclase-wehrlites and peridotites on the East Pacific Rise (Hess Deep) and the Mid-Atlantic Ridge (DSDP Site 334): evidence for magma percolation in the oceanic upper mantle. *Earth Planet. Sci. Lett.* **115**, 137–149.

Glueckauf E. (1955) Theory of Chromatography Part 10. Formula for diffusion into spheres and their application to chromatography. *Trans. Faraday Soc.* **51**, 1540–1551.

Hart S. R. (1993) Equilibration during mantle melting: a fractal tree model. *Proc. Natl. Acad. Sci.* **90**, 11914–11918.

Hellebrand E. and Snow J. E. (2003) Deep melting and sodic metasomatism underneath the highly oblique-spreading Lena Trough (Arctic Ocean). *Earth Planet. Sci. Lett.* **216**, 283–299.

Hellebrand E., Snow J. E., Dick H. J. B. and Hofmann A. W. (2001) Coupled major and trace elements as indicators of the extent of melting in mid-ocean-ridge peridotites. *Nature* **410**, 677–681.

Hellebrand E., Snow J. E., Hoppe P. and Hofmann A. W. (2002) Garnet-field melting and late-stage refertilization in residual abyssal peridotites from the central Indian ridge. *J. Petrol.* **43**, 2305–2338.

Hesse M., Schiemenz A., Liang Y. and Parmentier E. M. (2011) Compaction–dissolution waves in an upwelling mantle column. *Geophys. J. Int.* **187**, 1057–1075.

Hewitt I. J. (2010) Modelling melting rates in upwelling mantle. *Earth Planet. Sci. Lett.* **300**(264), 274.

Iwamori H. (1992) Melt-solid flow with diffusion-controlled chemical reaction. *Geophys. Res. Lett.* **19**, 309–312.

Iwamori H. (1993) A model for disequilibrium mantle melting incorporating melt transport by porous and channel flows. *Nature* **366**, 734–737.

Iwamori H. (1994) ^{238}U–^{230}Th–^{226}Ra and ^{235}U–^{231}Pa disequilibria produced by mantle melting and porous and channel flows. *Earth Planet. Sci. Lett.* **125**, 1–16.

Johnson K. T. M. and Dick H. J. B. (1992) Open system melting and temporal and spatial variation of peridotite and basalt at the Atlantis II Fracture Zone. *J. Geophys. Res.* **97**, 9219–9241.

Johnson K. T. M., Dick H. J. B. and Shimizu N. (1990) Melting in the oceanic upper mantle: an ion microprobe study of diopsides in abyssal peridotites. *J. Geophys. Res.* **95**, 2661–2678.

Kelemen P. B., Hirth G., Shimizu N., Spiegelman M. and Dick H. J. B. (1997) A review of melt migration processes in the adiabatically upwelling mantle beneath oceanic spreading ridges. *Phil. Trans. R. Soc. Lond.* **A355**, 282–318.

Kinzler R. J. and Grove T. L. (1992) Primary magmas of mid-ocean ridge basalts 1. Experiments and methods. *J. Geophys. Res.* **97**, 6885–6906.

Liang Y. (2003a) On the thermo-kinetic consequences of slab melting. *Geophys. Res. Lett.* **30**, 2270. http://dx.doi.org/10.1029/2003GL018969.

Liang Y. (2003b) Kinetics of crystal–melt reaction in partially molten silicates. 1. Grain scale processes. *Geochem. Geophys. Geosyst.* **4**, 1045. http://dx.doi.org/10.1029/2002GC000375.

Liang Y. (2008) Simple models for concurrent melting and melt migration in an upwelling heterogeneous mantle column: analytical solutions. *Geochim. Cosmochim. Acta* **72**, 3804–3821.

Liang Y. and Peng Q. (2010) Non-modal melting in an upwelling mantle column: steady-state models with applications to REE depletion in abyssal peridotites. *Geochim. Cosmochim. Acta* **74**, 321–339.

Liang Y., Schiemenz A., Hesse M., Parmentier E. M. and Hesthaven J. S. (2010) High-porosity channels for melt migration in the mantle: Top is the dunite and bottom is the harzburgite and lherzolite. *Geophys. Res. Lett.* **37**, L15306. http://dx.doi.org/10.1029/2010GL044162.

Liang Y., Schiemenz A., Hesse M. and Parmentier E. M. (2011) Waves, channels, and the preservation of chemical heterogeneities during melt migration in the mantle. *Geophys. Res. Lett.* **38**, L20308. http://dx.doi.org/10.1029/2011GL049034.

McKenzie D. (1985) ^{230}Th–^{238}U disequilibrium and the melting processes beneath ridge axes. *Earth Planet. Sci. Lett.* **72**, 149–157.

Müntener O., Manatschal G., Laurent D. and Pettke T. (2010) Plagioclase peridotites in ocean-continent transitions: refertilized mantle domains generated by melt stagnation in the shallow mantle lithosphere. *J. Petrol.* **51**, 255–294.

Navon O. and Stolper E. (1987) Geochemical consequences of melt percolation: The upper mantle as a chromatographic column. *J. Geol.* **95**, 285–307.

Niu Y. (2004) Bulk-rock major and trace element compositions of abyssal peridotites: implications for mantle melting, melt extraction and post-melting processes beneath mid-ocean ridges. *J. Petrol.* **45**, 2423–2458.

Niu Y. and Hèkinian R. (1997) Basaltic liquids and harzburgitic residues in the Garrett Transform: a case study at fast-spreading ridges. *Earth Planet. Sci. Lett.* **146**, 243–258.

Niu Y., Langmuir C. H. and Kinzler R. (1997) The origin of abyssal peridotites: a new perspective. *Earth Planet. Sci. Lett.* **152**, 251–265.

Prinzhofer A. and Allègre C. J. (1985) Residual peridotites and the mechanisms of partial melting. *Earth Planet. Sci. Lett.* **74**, 251–265.

Ozawa K. (2001) Mass balance equations for open magmatic systems: trace element behavior and its application to open system melting in the upper mantle. *J. Geophys. Res.* **106**, 13407–13434.

Qin Z. (1992) Disequilibrium partial melting model and its implications for trace element fractionations during mantle melting. *Earth Planet. Sci. Lett.* **112**, 75–90.

Quintard M. and Whitaker S. (1996) Transport in chemically and mechanically heterogeneous porous media. I: theoretical development of region-averaged equations for slightly compressible single-phase flow. *Adv. Water Resour.* **19**, 29–47.

Ribe N. M. (1985) The generation and composition of partial melting in the earth's mantle. *Earth Planet. Sci. Lett.* **73**, 361–376.

Richter F. M. and DaPaolo D. J. (1987) Numerical models for diagenesis and the Neogene Sr isotopic evolution of seawater from DSDP Site 590B. *Earth Planet. Sci. Lett.* **83**, 27–38.

Ross K. and Elthon D. (1993) Cumulates from strongly depleted mid-ocean-ridge basalt. *Nature* **365**, 826–829.

Rudge J. F., Bercovici D. and Spiegelman M. (2011) Disequilibrium melting of a two phase multicomponent mantle. *Geophys. J. Int.* **184**, 699–718.

Seyler M. and Bonatti E. (1997) Regional-scale melt–rock interaction in lherzolitic mantle in the Romanche Fracture Zone (Atlantic Ocean). *Earth Planet. Sci. Lett.* **146**, 273–287.

Seyler M., Toplis M. J., Lorand J.-P., Luguet A. and Cannat M. (2001) Clinopyroxene microtextures reveal incompletely extracted melts in abyssal peridotites. *Geology* **29**, 155–158.

Seyler M., Lorand J.-P., Dick H. J. B. and Drouin M. (2007) Pervasive melt percolation reactions in ultra-depleted refractory harzburgites at the Mid-Atlantic Ridge, 15°20′N: ODP Hole 1274A. *Contrib. Mineral. Petrol.* **153**, 303–319.

Shaw D. M. (2000) Continuous (dynamic) melting theory revisited. *Can. Mineral.* **38**, 1041–1063.

Shaw D. M. (2006) *Trace Elements in Magmas*. Cambridge Univ. Press, New York.

Shimizu N. (1998) The geochemistry of olivine-hosted melt inclusions in FAMOUS basalt ALV519-4-1. *Phys. Earth Planet. Interiors* **107**, 183–201.

Sobolev A. V. and Shimizu N. (1993) Ultra-depleted primary melt included in an olivine from the Mid-Atlantic Ridge. *Nature* **363**, 151–154.

Spiegelman M. and Kenyon T. (1992) The requirements for chemical disequilibrium during magma migraion. *Earth Planet. Sci. Lett.* **109**, 611–620.

Spiegelman M. and Kelemen P. B. (2003) Extreme chemical variability as a consequence of channelized melt transport. *Geochem. Geophys. Geosyst.* **4**(1055). http://dx.doi.org/10.1029/2002GC000336.

Sun C. and Liang Y. (2012) Distribution of REE between clinopyroxene and basaltic melt along a mantle adiabat: effects of major element composition, water, and temperature. *Contrib. Mineral. Petrol.* **163**, 807–823.

Sun C. and Liang Y. (2014) An assessment of subsolidus reequilibration on REE distribution among mantle minerals olivine, orthopyroxene, clinopyroxene, and garnet in peridotites. *Chem. Geol.* **372**, 80–91.

Takazawa E., Abe N., Seyler M. and Meurer W. P. (2007) Hybridization of dunite and gabbroic materials in Hole 1271B from mid-Atlantic ridge 15°N: implications for melt flow and reaction in the upper mantle, Kelemen, P. B. , Kikawa, E. and Miller, D. J. (eds.). *Proc. ODP, Sci. Results*, College Station, TX (Ocean Drilling Program) **209**, 1–23. http://dx.doi.org/10.2973/odp.proc.sr.209.005.2007.

Tartarotti P., Susini S., Nimis P. and Ottolini L. (2002) Melt migration in the upper mantle along the Romanche Fracture Zone (Equatorial Atlantic). *Lithos* **63**, 3–4.

Van Orman J. A., Grove T. L. and Shimizu N. (2001) Rare earth element diffusion in diopside; influence of temperature, pressure, and ionic radius, and an elastic model for diffusion in silicates. *Contrib. Mineral. Petrol.* **141**, 687–703.

Van Orman J. A., Grove T. L. and Shimizu N. (2002) Diffusive fractionation of trace elements during production and transport of melt in Earth's upper mantle. *Earth Planet. Sci. Lett.* **198**, 93–112.

Vermeulen T. (1953) Theory for irreversible and constant-pattern solid diffusion. *Ind. Eng. Chem.* **45**, 1664–1670, 1953.

Warren J. M. and Shimizu N. (2010) Cryptic variations in abyssal peridotite compositions: evidence for shallow-level melt infiltration in the oceanic lithosphere. *J. Petrol.* **51**, 395–423.

Weatherley S. M. and Katz R. F. (2012) Melting and channelized magmatic flow in chemically heterogeneous, upwelling mantle. *Geochem. Geophys. Geosyst.* **13**, Q0AC18. http://dx.doi.org/10.1029/2011GC003989.

Whitaker S. (1999) *The Method of Volume Averaging*. Kluwer Academic Publishers, Dordrecht.

Workman R. K. and Hart S. R. (2005) Major and trace element composition of the depleted MORB mantle (DMM). *Earth Planet. Sci. Lett.* **231**, 53–72.

Yao L., Sun C. and Liang Y. (2012) A parameterized model for REE partitioning between low-Ca pyroxene and basaltic melts with applications to adiabatic mantle melting and pyroxenite-derived melt and peridotite interaction. *Contrib. Mineral. Petrol.* **164**, 261–280.

Zou H. (1998) Trace element fractionation during modal and nonmodal dynamic melting and open-system melting: a mathematical treatment. *Geochim. Cosmochim. Acta* **62**, 1937–1945.

Associate editor: Wolfgang Bach